Ultrasound in Med. & Biol., Vol. 41, No. 10, pp. 2700–2713, 2015

0301-5629/$ - see front matter

http://dx.doi.org/10.1016/j.ultrasmedbio.2015.06.003

● *Original Contribution*

HIGH-FREQUENCY ACOUSTIC IMPEDANCE IMAGING OF CANCER CELLS

Muhannad N. Fadhel, Elizabeth S. L. Berndl, Eric M. Strohm, and Michael C. Kolios
Department of Physics, Ryerson University, Toronto, Ontario, Canada

(*Received* 3 *December* 2014; *revised* 14 *May* 2015; *in final form* 2 *June* 2015)

Abstract—Variations in the acoustic impedance throughout cells and tissue can be used to gain insight into cellular microstructures and the physiologic state of the cell. Ultrasound imaging can be used to create a map of the acoustic impedance, on which fluctuations can be used to help identify the dominant ultrasound scattering source in cells, providing information for ultrasound tissue characterization. The physiologic state of a cell can be inferred from the average acoustic impedance values, as many cellular physiologic changes are linked to an alteration in their mechanical properties. A recently proposed method, acoustic impedance imaging, has been used to measure the acoustic impedance maps of biological tissues, but the method has not been used to characterize individual cells. Using this method to image cells can result in more precise acoustic impedance maps of cells than obtained previously using time-resolved acoustic microscopy. We employed an acoustic microscope using a transducer with a center frequency of 375 MHz to calculate the acoustic impedance of normal (MCF-10 A) and cancerous (MCF-7) breast cells. The generated acoustic impedance maps and simulations suggest that the position of the nucleus with respect to the polystyrene substrate may have an effect on the measured acoustic impedance value of the cell. Fluorescence microscopy and confocal microscopy were used to correlate acoustic impedance images with the position of the nucleus within the cell. The average acoustic impedance statistically differed between normal and cancerous breast cells (1.636 ± 0.010 MRayl vs. 1.612 ± 0.006 MRayl), indicating that acoustic impedance could be used to differentiate between normal and cancerous cells. (E-mail: mkolios@ryerson.ca) © **2015 World Federation for Ultrasound in Medicine & Biology.**

Key Words: **Acoustic impedance, Breast cancer cells, Acoustic impedance imaging, Acoustic microscopy.**

INTRODUCTION

Ultrasound wave interactions with homogeneous spherical or cylindrical objects are a well-understood phenomenon (Faran 1951). The acoustic impedance (in the case of a plane wave in an inviscid fluid medium) is equal to the product of density and speed of sound (Cobbold 2007). However, ultrasound wave interactions with cells and their complex microstructure are not as well understood (Mamou et al. 2008). Variations in acoustic impedance throughout the cell can alter ultrasound scattering interactions (Mamou et al. 2005, 2008), which can be used to detect anatomic and physiologic changes in tissues.

Changes in mechanical properties have been used to obtain information about the physiology and environment of cells (Suresh et al. 2005; Weiss et al. 2007). Mechanical properties are sensitive to changes in density, speed of sound or elastic properties of the cell at the length scale of the interrogating wavelength of ultrasound (Kolios 2009). Physiologic changes in the cell, including cell division, cell motility, cell adhesion, gene expression, signal transduction, apoptosis and the maturation of parasites in red blood cells, have been linked to changes in the elastic properties of the cell (Bao and Suresh 2003; Fuchs and Weber 1994; Ingber 2002; Weiss et al. 2007).

Acoustic impedance fluctuations can be used to acquire information about the tissue anatomic structures through calculation of the backscatter coefficient (BSC) (Mamou et al. 2005, 2008). The BSC is dependent on the relationship between an incident ultrasound wave of a particular wavelength, acoustic parameters (such as the density and speed of sound) and the size of the scattering object. The BSC has been used to characterize tissue microstructures in ocular, myocardial, liver and kidney tissues (Insana et al. 1992; Lizzi et al. 1983, 1987; Wear 1987). Additionally, maps of the spatial distribution of the BSC were used to monitor high-intensity focused ultrasound (HIFU)

Address correspondence to: Michael C. Kolios, Department of Physics, Ryerson University, 350 Victoria Street, Toronto, Ontario M5B 2K3, Canada. E-mail: mkolios@ryerson.ca

treatments (Kemmerer et al. 2010), detect abnormal lymph nodes (Mamou et al. 2011), differentiate between cancer tissues (Hruska et al. 2009; Oelze et al. 2004) and identify various forms of cell death (Kolios et al. 2002, 2003). In some cases, the BSC could not be used to identify breast cancers, although the optical images displayed a clear difference in the cellular microstructure (Oelze and Zachary 2006). Currently there is no consensus on the dominant ultrasonic scattering source of biological structures. Some studies support the hypothesis that the whole cell acts as a dominant scatterer source (Falou et al. 2010; Oelze and Zachary 2006). Other studies suggest that the nucleus is the main scatterer source when cells are embedded in tumors or surrounded by other cells (Czarnota et al. 1999; Kolios et al. 2003; Taggart et al. 2007). Thus, acoustic impedance fluctuations can be used to identify the dominant tissue scattering source, improving the diagnostic and monitoring capabilities of ultrasound. An understanding of the shape and mechanical properties of biological structures using acoustic impedance maps can provide information that can aid ultrasound tissue characterization.

Breast tumors are the most common malignant tumor in the world among women (Carkaci et al. 2011). Ultrasound can be used to detect these tumors; sonography is used to detect changes in mechanical properties (Carkaci et al. 2011; Mathis 2011). The detected changes in ultrasound contrast are not always due to tumor growth; therefore, biopsies are used for confirmation. A biopsy is an invasive, expensive and time-consuming procedure; a non-invasive method of determining malignancy has an impact on the diagnosis of breast tumor (Mamou et al. 2005; Tohno et al. 2009). An understanding the mechanical properties of normal and cancerous breast cells can be used to better analyze the ultrasound signals acquired from sonography and, in principle, increase its sensitivity in identifying tumors.

Hozumi et al. (2005) developed the acoustic impedance imaging method (AIIM), which has been used to create acoustic impedance maps of tissues. This method assumes that the dimensions of the scattering source are significantly larger than the ultrasound wavelength and the incident angle is normal to the surface of the tissue. Under these assumptions, the reflection coefficient caused by impedance mismatch between fluid–fluid interfaces can be simplified to

$$R = \frac{Z_2 - Z_1}{Z_2 + Z_1} \tag{1}$$

where Z_1 and Z_2 are the acoustic impedances of the first and second fluids, respectively. The AIIM uses a reference material with a known acoustic impedance to measure the impedance of the sample (Hozumi et al. 2005). The sample is attached to a solid substrate with known properties (*e.g.*, polystyrene). In the case of a solid–fluid or fluid–solid interface with a defined incident angle to the surface, the reflection coefficient equation must account for the formation of shear waves in the solid layer (Hozumi et al. 2007; Mayer 1965). Also, the presence of multiple impedance mismatches within a short range (of the order of the ultrasound wavelength) will have an impact on the measured acoustic impedance.

Many techniques have been developed to measure the mechanical properties of biological structures, such as atomic force microscopy (Radmacher et al. 1995), magnetic tweezers (Puig-De-Morales et al. 2001), optical tweezers (Ashkin and Dziedzic 1987), micropipette aspiration (Chapman 1982), shear-flow methods (Usami et al. 1993) and stretching devices (Wang et al. 2000). These techniques apply stress on the biological structures to measure its mechanical properties. Acoustic microscopy is desirable because of the minimal stress it applies to the sample and the relatively high resolution and speed (Kundu et al. 2000). The backscattered signal can be analyzed in the time domain or frequency domain (Kundu et al. 2000; Weiss et al. 2007). Time-domain analysis can be used to measure the speed of sound and calculate the acoustic impedance of the sample. The speed of sound is measured from the time shift between the sample and the reference, whereas the acoustic impedance is measured from the amplitude change between the sample and the reference (Strohm et al. 2010; Weiss et al. 2007). Frequency-domain analysis can be used to measure the density and speed of sound from the phase analysis or interpolation of the voltage-versus-frequency plot (Kundu et al. 1991, 2000; Zhao et al. 2012). The acoustic impedance of single cells has been measured using time-resolution techniques on HeLa and fibroblast cells (Briggs et al. 1993; Hildebrand and Rugar 1984; Weiss et al. 2007). The setups for these experiments create an angle between the transducer and the cell surface that was not accounted for because of the difficulty in determining this angle. The variation in the angle will affect the measured acoustic impedance values. In contrast, the AIIM is the only proposed method that can be used to measure acoustic impedance maps of single cells and accounts for the angle between the transducer and cell surface by changing the setup to create a 90° angle between the transducer and the cell surface.

The main objective of this study was to use high-frequency ultrasound to calculate the acoustic impedance maps of normal and cancerous breast cells using the AIIM. The acoustic impedance values are calibrated to account for the incident angle of the transducer and the

shear waves created in the substrate. This will help in understanding the mechanical properties of individual normal and tumor breast cells and potentially identify dominant scattering sources in breast tissues.

METHODS

Cell preparation

In this study, normal and cancerous cell cultures were used. MCF-10 A cells, a human breast epithelial cell line (ATCC, Manassas, VA, USA), were grown in mammary epithelial cell growth medium with cholera toxin (100 ng/mL), fetal bovine serum (FBS) (2% v/v), hydrocortisone (0.04% v/v), human fibroblast growth factor basic (0.4% v/v), vascular endothelial growth factor (0.1% v/v), R3 IGF-1 (0.1% v/v), ascorbic acid (0.1% v/v), human fibroblast growth factor (0.1% v/v) and heparin (0.1% v/v) (Lonza, ON, Canada). MCF-7 cells, a human invasive breast duct carcinoma (ATCC), were grown in Dulbecco's modified Eagle's medium (DMEM) (Sigma–Aldrich, ON, Canada) supplemented with FBS (10% v/v) (Sigma–Aldrich, prepared at Princess Margaret Hospital, Toronto, ON, Canada). Both cell lines were kept in a humidified incubator maintained at 37°C and 5% CO_2. Cells were maintained in the exponential growth phase and passaged using trypsin dissociation when the flasks were 80%–90% confluent.

Twenty-four hours before the experiment, 300,000 cells in 10 mL of medium were transferred to an Opticell culture system, made of two parallel polystyrene thin membranes (NUNC Opticell, Thermo Fisher Scientific, Waltham, MA, USA). The Opticell was kept in the incubator for the cells to adhere to the membrane.

Two hours before the experiment, the medium was replaced with 5–25 μM CellTracker Orange (Life Technologies, Carlsbad, CA, USA) in growth medium to stain the cytoplasm. The Opticell was incubated for 30 min, washed with phosphate-buffered saline (PBS) and then incubated with Hoechst 33342 (Life Technologies) for 30 min.

Data collection

Acoustic and fluorescence data. A custom-built scanning acoustic microscope (SASAM, Kibero, Saarbrucken, Germany) capable of simultaneous acoustic and fluorescence imaging was used in these experiments. Acoustic imaging was completed using a transducer with a center frequency of 375 MHz, a bandwidth of 150 MHz and an aperture angle of 60°. The axial resolution (R_{ax}) and lateral resolution (R_{lat}) of the transducer in the water were calculated to be 5.1 and 3.6 μm, respectively, using equations derived elsewhere for a spherical radiating transducer at the focus (Foster et al. 2000).

Fluorescence microscopy images were taken with a monochrome CCD camera with a resolution of 1392 × 1040 pixels (Lumenera, Ottawa, ON, Canada). The experimental setup (Fig. 1) was kept in a climate-controlled chamber at 36.0 ± 0.2°C. The Opticell was coupled to the transducer using degassed water (Fig. 1a) and was positioned so that the cells were upside down relative to the transducer (Fig. 1b).

Samples were imaged both acoustically and optically. Ultrasound backscatter radiofrequency signals were obtained by scanning the transducer in the x–y plane with a step size of 1 μm and an area ranging from 40 to 100 μm depending on cell size. Single and clustered MCF-7 and MCF-10 A cells were imaged. Clustered cells were defined as two or more cells attached together side by side (no separation detectable on the microscope images). Single cells were defined as cells not attached to other cells. Other studies have indicated that cells

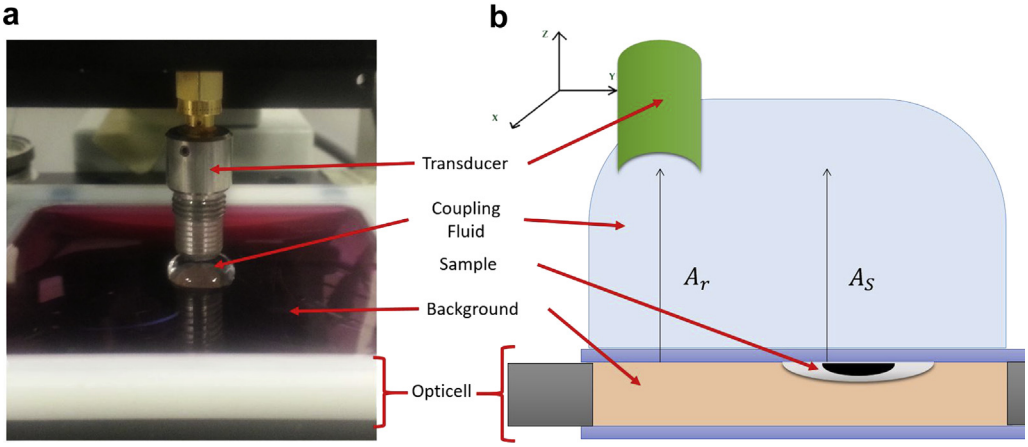

Fig. 1. (a) Setup for the AIIM experiment with the transducer positioned above the sample. (b) Schematic of the acoustic microscopy setup. AIIM = acoustic impedance imaging method.

attached to each other can alter cell mechanical properties. In case of MCF-7 cells, 20 single and 10 clustered cells were imaged using both acoustic and fluorescence microscopy. In the case of MCF-10 A cells, 15 single and 13 clustered cells were imaged using both acoustic and fluorescence microscopy.

After the cells were imaged using the acoustic microscope, the medium in the Opticell was replaced with 10% formalin for 15 min to fix the cells and then replaced with PBS. The clustered cells previously imaged before fixation were re-imaged after fixation. Seven MCF-7 and 7 MCF-10 A cells were retained, as some of the cells were lost when the Opticell was washed. The results for the clustered-fixed cells were compared with those for the clustered-live cells.

Confocal images. A confocal scanning microscope (LSM 700, Zeiss, Oberkochen, Germany) with 40× oil lens was used to obtain 3-D images of MCF-7 and MCF-10 A cells stained with Hoechst and CellTracker Orange to image the nucleus and cytoplasm, respectively. Cells were imaged through their entire volume using an axial step size of 0.33 μm.

Data processing

Acoustic impedance calibration. The maximum amplitudes of the reflected radiofrequency signals (A_r) were processed to obtain acoustic impedance maps. To calculate the amplitude of the incident signal (A_r), we used the equation

$$A_r = \frac{A_0(Z_{PE_l} - Z_r)}{(Z_{PE_l} + Z_r)} \tag{2}$$

where A_r is the amplitude of the reflected signal caused by the impedance mismatch between the polystyrene substrate and the reference, Z is the acoustic impedance and the subscripts PE, r and 1 refer to the polystyrene substrate, reference and longitudinal wave, respectively. The apparent acoustic impedance of the sample (Z_{S_a}) was found using

$$A_s = \frac{A_0(Z_{PE_l} - Z_{s_a})}{(Z_{PE_l} + Z_{s_a})} \tag{3}$$

where A_s is the amplitude of the reflected signal caused by the impedance mismatch between the polystyrene substrate and the sample. This equation does not account for the shear waves and the finite angle of the transducer.

To account for the shear waves and the angle of the transducer, a calibration is applied to find the acoustic impedance of the sample (Z_{S_t}). This was done by substituting A_0 from eqn (2) into eqn (3) and rearranging it to solve for Z_{S_a}:

$$Z_{S_a} = \frac{1 + \frac{A_s}{A_r}\frac{Z_r - Z_{PE_l}}{Z_r + Z_{PE_l}}}{1 - \frac{A_s}{A_r}\frac{Z_r - Z_{PE_l}}{Z_r + Z_{PE_l}}} Z_{PE_l} \tag{4}$$

A_s/A_r in the eqn (4) assumes fluid–fluid boundaries (no shear waves) with normal incident angle. To eliminate these assumptions, A_s/A_r is calculated using the equation

$$\frac{A_s(Z_{s_t}, c_s, \theta_a)}{A_r(Z_{r_t}, c_r, \theta_a)} = \frac{\int_0^{\theta_a} T_{c-PE}(\theta) R_{PE-s}(Z_{s_t}, c_s, \theta) T_{PE-c}(Z_{s_t}, c_s, \theta) d\theta}{\int_0^{\theta_a} T_{c-PE}(\theta) R_{PE-r}(Z_{r_t}, c_r, \theta) T_{PE-c}(Z_{r_t}, c_r, \theta) d\theta} \tag{5}$$

where θ_a is one-half the aperture angle of the ultrasound transducer, c_s and c_r are the longitudinal speed of sound of the sample and reference, T_{c-PE} is the signal transmitted from the interface between the coupling fluids to the polystyrene substrate, R_{PE-s} or R_{PE-r} is the reflected signal at the polystyrene substrate and sample or reference boundary and T_{PE-c} is the signal transmitted from the polystyrene substrate to the coupling fluid. These interfaces are solid–fluid or fluid–solid. The equations describing the amplitude of the reflected and transmitted ultrasound pulse incident on solid–fluid or fluid–solid have been derived by Mayer (1965) (see Appendix). These equations were used to calculate T_{c-PE}, R_{PE-s}, R_{PE-r} and T_{PE-c}. The speed of sound c_s was calculated by dividing Z_{s_t} by the density of the target, which is assumed to be 1 g/cm^3. The integral in eqn (5) is computed through the summation of angle (θ) at intervals of 0.01°.

To confirm this calibration at intervals 1.40–1.80 MRayl, the acoustic impedance of the degassed water was measured using air as a reference (c_{air} = 352 m/s, Z_{air} = 0.0004 MRayl) (Hozumi et al. 2005). This was done by applying the AIIM on a sample of degassed water. Four different samples were prepared using four different Opticells. Each sample was imaged at five different locations of dimensions 50 × 50 μm with 2-μm step size. The same method was used to measure the acoustic impedance of the MCF-7 medium, the MCF-10 A medium and the PBS, as they were the background of the live and fixed cells. The background speed of sound is a required

parameter for the calibration (eqn 4). The speed of sound of the medium and the PBS were calculated by dividing the measured true acoustic impedance by the density. The density of the liquids was measured by dividing the mass by the volume using an electronic balance (Scientech, Boulder, CO, USA) and a 5-mL pipet (Fisher Scientific, Ottawa, ON, Canada).

Size comparison. The fluorescence images of the cytoplasm and nucleus, stained with CellTracker Orange and Hoechst, respectively, and the calibrated acoustic impedance maps were superimposed for each of the 20 single-cell samples. A trace line was selected at a location within the image where the difference between the cell diameter and the nucleus diameter, as assessed through fluorescent staining, was greatest. This was done to detect possible differences in the acoustic impedance values of the cytoplasm and nucleus. From each trace line, the size was calculated using the full width at half-maxima. The size ratios of fluorescence images labeled with CellTracker Orange to acoustic impedance images and of fluorescence images labeled with Hoechst stain to acoustic impedance images were acquired. These calculations were done for the 20 single-live MCF-7 cells.

Average acoustic impedance values of cells. The acoustic impedance images of the cells were segmented from the background using thresholding and erosion. Background impedance was eliminated by applying global thresholds of 1.575 and 1.565 MRayl for both medium and PBS backgrounds, respectively. Erosion with 3- and 7-μm disks, equivalent to one and two times the lateral resolution of the transducer in the polystyrene substrate, was done to reduce the effect of the point spread function of the transducer on the measured acoustic impedance values. The mean and standard deviation of the non-eliminated pixels were calculated for MCF-7 versus MCF-10 A and 3 μm versus 7 μm erosion disks for the three different groups: single-live, clustered-live and clustered-fixed cells. The means of the different groups were compared in MATLAB (The MathWorks, Natick, MA, USA) using analysis of variance followed by a multiple comparison test ($\alpha = 0.05$) and Tukey–Kramer *post hoc* test). The means of each image were used as data points for the groups to examine statistical differences.

Confocal processing. Each stack of confocal images was analyzed to identify the distance between the polystyrene substrate and the nucleus. The cells were fixed to preserve their gross architecture (Chesnick et al. 2010; Gillespie et al. 2002). The first layer with CellTracker Orange stain was identified as the location of the polystyrene substrate, and the first layer with Hoechst stain indicated the depth of the nucleus. Sixteen MCF-7 and 16 MCF-10 A cells were imaged confocally to obtain a distribution of values representing the distance of the nucleus from the polystyrene substrate.

Simulations

To better understand the effect of the distance of microstructures from the polystyrene substrate on the measured acoustic impedance, simulations were performed (COMSOL MultiPhysics, Stockholm, Sweden). This software uses the acoustic wave equation to solve for the scattered pressure. Three different material domains were used in the finite-element software to simulate the polystyrene substrate, the cytoplasm and the nucleus of a cell in one dimension. Three different mechanical properties were assigned to each different domain, as outlined in Table 1. These properties represent published acoustic impedances vales of the nucleus (1.6–1.7 MRayl) and the cytoplasm (1.6 MRayl) (Kundu et al. 1991, 2000; Mamou et al. 2005; Weiss et al. 2007). In the simulations, the thickness of the cytoplasmic domain was varied between 0.05 and 4.00 μm, with a step size of 0.05 μm to represent the change in nucleus location. The polystyrene substrate and the nucleus domains were 30.0 μm thick. The maximum element size was set at 0.01 μm. To simulate the incident pressure pulse generated by the transducer, we used the following equation, which represents a pulsed plane wave to approximate the incident wave at the focal spot of the spherically focused transducer:

$$p_i(z,t) = -A\sin\left(2\pi f_o\left(t-\frac{z}{v}\right)\right)\exp\left(-4\left(f_{BW}\left(t-\frac{z}{v}\right)\right)^2\right) \quad (6)$$

Here, p_i is the incident pressure function, A is the amplitude of the negative peak pressure (1 MPa), f_o is

Table 1. Parameters used to simulate three consecutive layers with different densities and speeds of sound*

	Layer 1 (polystyrene substrate)			Layer 2 (cytoplasm)			Layer 3 (nucleus)		
Simulation	Density (kg/m^3)	Speed of sound (m/s)	Impedance (MRayl)	Density (kg/m^3)	Speed of sound (m/s)	Impedance (MRayl)	Density (kg/m^3)	Speed of sound (m/s)	Impedance (MRayl)
1	1050	2340	2.46	1032	1550	1.60	1035	1555	1.61
2	1050	2340	2.46	1032	1550	1.60	1048	1575	1.65
3	1050	2340	2.46	1032	1550	1.60	1062	1600	1.70

* Layers 1, 2 and 3 are used to represent the properties of polystyrene substrate, cytoplasm and nucleus.

the central frequency (375 MHz), v is the speed of sound in water (1520 m/s), f_{BW} is the bandwidth of the transducer (150 MHz) and t and z are the modeled time and spatial variables, respectively. The time step used was 33 ns with a relative tolerance of 5 μs. The spatial variable was set to start at -20 μm to include the whole incident pressure pulse in the simulations, as a value of 0 μm will simulate half of the incident pulse. The maximum amplitude of the reflected signal was calculated. The reflected pressure was replaced by acoustic impedance (Z_2) using the equation

$$\frac{p_r}{p_i} = \frac{Z_2 - Z_{PE}}{Z_2 + Z_{PE}} \tag{7}$$

where p_i and p_r are the amplitude of the incident and reflected signals, and Z_{PE} is the acoustic impedance of the polystyrene substrate. The calculated Z_2 versus thickness of the middle layer, representing the cytoplasm thickness between the polystyrene substrate and the nucleus, was plotted.

RESULTS

The acoustic impedance values of normal and cancer breast cells were obtained using the AIIM. Fluorescence confocal images were used both to assess the morphology of a cell and to calculate the distance between the nucleus and the polystyrene substrate. The simulations were run to determine the effect of the distance between the nucleus and the polystyrene substrate on the measured 2-D acoustic impedance images.

Calibrated acoustic impedance images

Representative radiofrequency signals collected from the middle of a MCF-7 cell and from a location within the medium (background) are illustrated in Figure 2a.

A correction factor was required to account for the shear waves created in the polystyrene substrate. Acoustic impedance calibration plots are provided in Figure 2b for air, medium and PBS used as the reference. The densities for the MCF-7 medium, the MCF-10 A medium and the PBS were measured to be 0.992 ± 0.012, 0.990 ± 0.010 and 1.004 ± 0.010 g/cm^3 at 36°C. The accuracy of the AIIM was tested by measuring the acoustic impedance of water. The measured acoustic impedance of the water, the MCF-7 medium, the MCF-10 A medium and the PBS were 1.517 ± 0.006, 1.549 ± 0.006, 1.546 ± 0.006 and 1.541 ± 0.006 MRayl, respectively. Comparison of the measured acoustic impedance of water with the literature value of 1.512 MRayl yields an error of 0.33% (Temkin 1981).

Size comparison

Acoustic impedance images of live-clustered MCF-10 A cells and the effect of threshold and erosion on the image are illustrated in Figure 3. Representative fluorescence microscopy images, calibrated 2-D acoustic impedance maps of MCF-7 and MCF-10 A cells produced using the AIIM and line traces of single cells are in Figures 4 and 5, respectively. In some cases, the acoustic impedance images could be used to determine the presence of the nucleus (Figs. 4 and 5, rows I and II). This detection was based on an increase (Figs. 4 and 5, row I) or decrease (Figs. 4 and 5, row II) in the measured acoustic impedance. In other cases, we were unable to detect the presence of the nucleus on acoustic impedance images (Figs. 4 and 5, row III).

To determine whether the highest acoustic impedance change occurs at the medium–cytoplasm boundary or the cytoplasm–nucleus boundary, the sizes of the

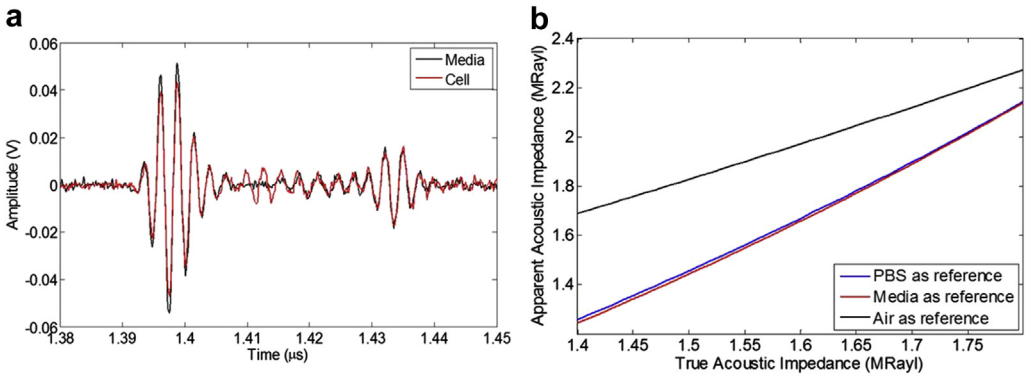

Fig. 2. (a) Plot comparing the radiofrequency signal reflected from a location corresponding to the middle of a cell (*red*) with the radiofrequency signal reflected from the medium (*black*). (b) AIIM calibration plot. Parameters used: $Z_{PE_l} = 2.46$ MRayl, $c_{PE_t} = 1150$ m/s, $c_{PE_l} = 2340$ m/s, $c_{air} = 352$ m/s, $Z_{air} = 0.0004$ MRayl (Hozumi et al. 2005). PBS = phosphate-buffered saline; AIIM = acoustic impedance imaging method.

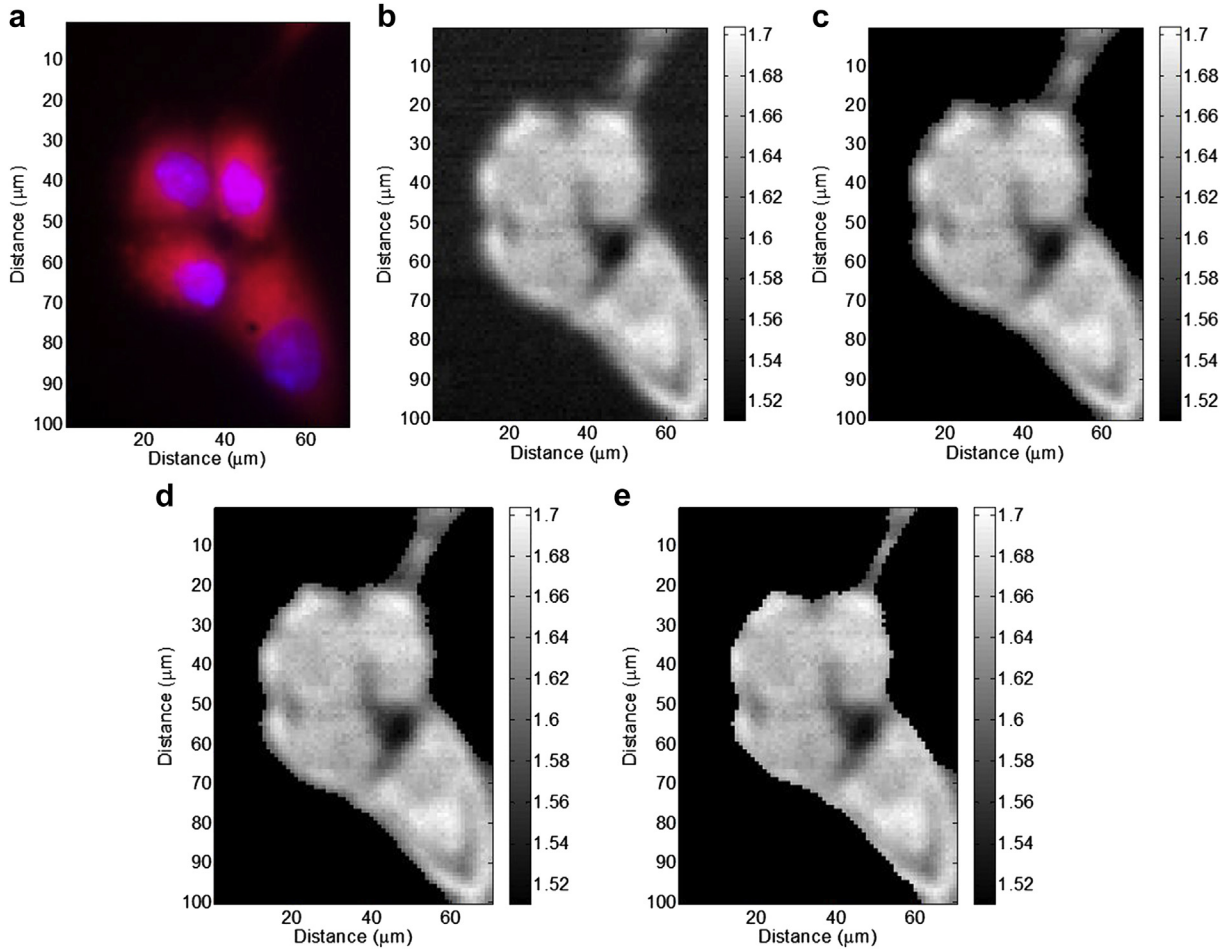

Fig. 3. Image processing of the acoustic impedance maps. (a) Fluorescence image of clustered-live MCF-10 A cells. (b) Acoustic impedance image of the same MCF-10 A cells. (c). Same cells as in (b) after applying the threshold. (d) Same cells as in (c) after applying 3-μm erosion disk. (e) Same cells as in (c) after applying 7-μm erosion disk.

structures were derived. Size was estimated from the full width at half-maximum of the trace lines of the (i) acoustic impedance images and (ii) fluorescence images labeled with Hoechst and CellTracker Orange for 20 single MCF-7 cells. The average size ratio of fluorescence images labeled with CellTracker Orange to acoustic impedance images was 1.02 $\pm$ 0.08. The average size ratio of fluorescence images labeled with Hoechst to acoustic impedance images was 0.63 $\pm$ 0.11.

Acquiring the average acoustic impedance of cells

Threshold and erosion operations were applied to all of the corrected acoustic impedance images of cells to segment the cells from the background. The average acoustic impedance and standard deviation of the segmented MCF-7 and MCF-10 A cells, after application of the threshold and 3- or 7-μm-diameter erosion disks, are listed in Table 2 and illustrated in Figure 6 for single-live, clustered-live and fixed-live cells. The *red plus signs* in Figure 6 represent data outliers. Means were compared using multiple comparison tests. The results indicate that the four different groups of single cells differed statistically. This includes MCF-7 versus MCF-10 A and 3-μm versus 7-μm erosion disk. In the case of clustered cells, statistical differences were observed between MCF-7 and MCF-10 A cells, but not between values obtained using the 3- and 7-μm erosion disks. Comparing the single, clustered and fixed cells. The results reveal a statistically significant decrease in the acoustic impedance value in the case of fixed cells. Clustered cells had a higher average acoustic impedance value than single cells, but the difference was not statistically significant.

Confocal images

Sixteen MCF-7 and 16 MCF-10 A fixed cells were imaged using confocal microscopy and stained with both Hoechst and CellTracker Orange. The average depth of the nucleus from the polystyrene substrate was calculated to be 0.60 $\pm$ 1.40 μm (MCF-7) and 0.35 $\pm$ 0.51 μm

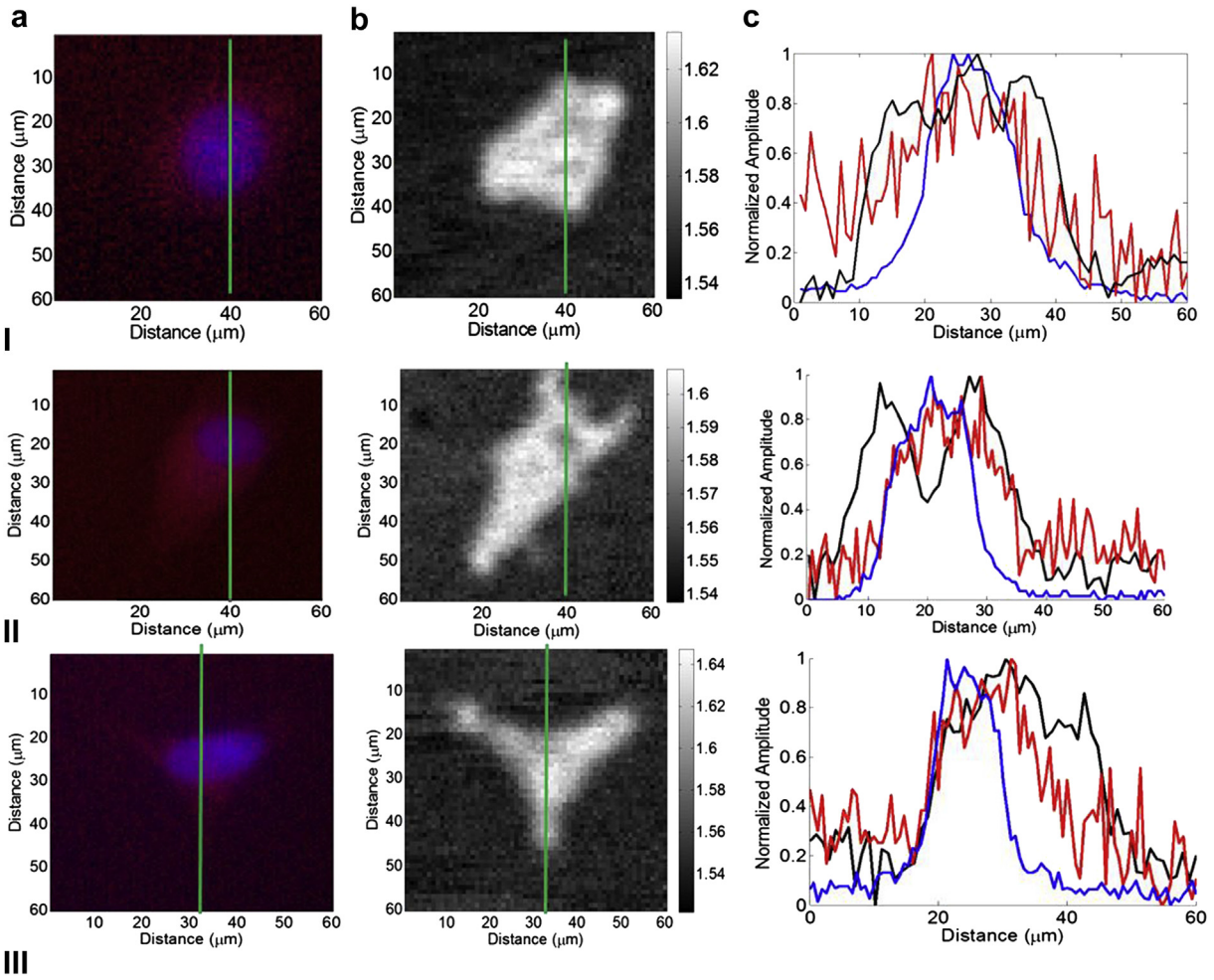

Fig. 4. Comparison of acoustic impedance images with fluorescence images of MCF-7 cells. (a) Fluorescence images of three single cells (I, II, III) acquired using Hoechst and CellTracker Orange stains pseudo-colored with blue and red, respectively. (b) Same cells imaged using the AIIM. (c) Values measured at the location indicated by the trace of the green lines of the normalized acoustic impedance (*black line*), and normalized intensity of the Hoechst and CellTracker Orange stains (*blue and red*, respectively) at the locations denoted in the images in (a) and (b). AIIM = acoustic impedance imaging method.

(MCF-10 A). Cross-sectional images of two MCF-7 cells are provided in Figure 7a.

Simulations

In Figure 7b are the results from COMSOL simulations. The figure illustrates the effect of two consecutive acoustic impedance mismatches on the AIIM. The acoustic impedance value measured using the AIIM will change as the depth of the nucleus from the polystyrene substrate changes to reflect an increase in, decrease in or no effect on the measured acoustic impedance value. When the acoustic impedance of the nucleus was greater than that of the cytoplasm, an increase in the measured acoustic impedance value occurred at distance ranges between 0 and 0.5 μm and between 1.5 and 2.5 μm, a decrease occurred at 0.5–1.5 and 2.5–3.5 μm and no change occurred at 0.5, 1.5, 2.5 and 3.5 μm (Fig. 7b).

DISCUSSION

Multiple features can be extracted by comparing the radiofrequency signals reflected from the cancerous cell and the medium (Fig. 2a). The signals used to generate the acoustic impedance images occurred at the location of the boundary between the substrate and the sample (at 1.390–1.405 μs in Fig. 2a). This signal is due to the acoustic impedance mismatch between the polystyrene substrate and the sample. The amplitude of the signal reflected from the cell is less than the amplitude of the signal reflected from the medium. This is because the acoustic impedance mismatch between the polystyrene substrate

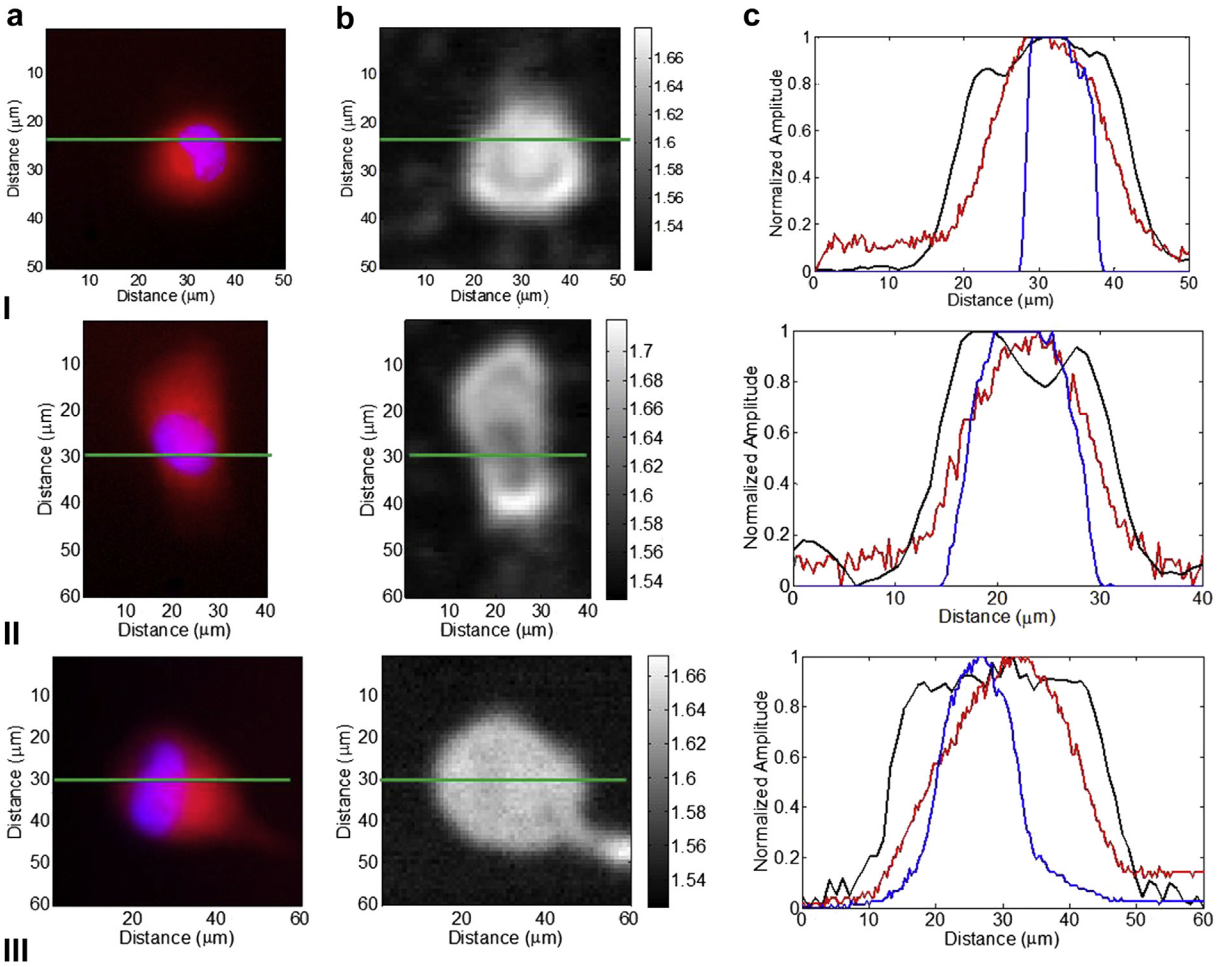

Fig. 5. Comparison of acoustic impedance images with fluorescence images of MCF-10 A cells. (a) Fluorescence images of three single cells (I, II, III) acquired using Hoechst and CellTracker Orange stains pseudo-colored with blue and red, respectively. (b) Same cells imaged using the AIIM. (c) Values measured at the location indicated by the trace of the green lines of the normalized acoustic impedance (*black line*), and normalized intensity of the Hoechst and CellTracker Orange stains (*blue and red*, respectively) at the locations denoted in the images in (a) and (b). AIIM = acoustic impedance imaging method.

and the cell is less than that between the polystyrene substrate and the medium. The signal recorded at 1.405–1.415 μs is due to the acoustic impedance mismatches within the sample (the cell). The signal recorded at 1.420–1.440 μs is potentially due to the leaky Rayleigh waves created in the coupling fluid and the polystyrene substrate (Maev 2008).

The setup for the experiment requires propagation of the ultrasound waves through the polystyrene substrate before the waves reach the sample. A calibration was applied to account for the finite angle of the transducer as the ultrasound waves enter the polystyrene substrate, as well as for the shear waves created in the polystyrene

Table 2. Average acoustic impedance and standard deviation of MCF-7 and MCF-10 A single-live, clustered-live and clustered-fixed cells using both 3- and 7-μm disk erosion

	Average acoustic impedance (MRayl)			
	MCF-7 cells		MCF-10 A cells	
	3-μm disk erosion	7-μm disk erosion	3-μm disk erosion	7-μm disk erosion
Single-live	1.600 ± 0.006	1.612 ± 0.006	1.627 ± 0.009	1.636 ± 0.010
Clustered-live	1.612 ± 0.008	1.619 ± 0.009	1.634 ± 0.009	1.641 ± 0.009
Clustered-fixed	1.572 ± 0.004	1.578 ± 0.004	1.580 ± 0.005	1.589 ± 0.007

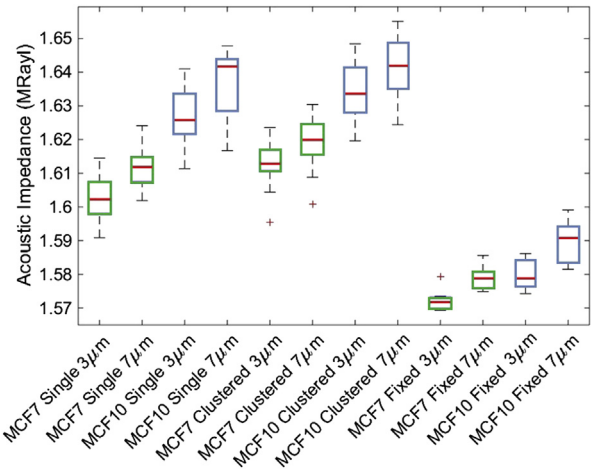

Fig. 6. Boxplot comparing the acoustic impedance values of MCF-7 cells (*green box*) with those of MCF-10 A cells (*blue box*) and the values of 3-μm erosion disks with those of 7-μm erosion disks for single-live, clustered-live and clustered-fixed cells. The *central red marks* are medians, the edges of the *blue and green boxes* are the 25th and 75th percentiles and the *whiskers* are the maximum and minimum values not including the outliers, which are represented by *red plus signs*.

substrate. The relation before applying the calibration (apparent acoustic impedance) and after applying the calibration (true acoustic impedance) is illustrated in Figure 2b. The apparent acoustic impedance and the true acoustic impedance are equal at the acoustic impedance of the reference (Z_r). In the case of the MCF-7 medium (*red*), PBS (*blue*) or air (*black*) as a reference, the apparent and true acoustic impedances coincide at 1.549, 1.541 or 0.0004 MRayl, respectively. In addition, by extrapolation, the three curves in Figure 2b intersect at the apparent acoustic impedance of 2.46 MRayl. This intersection occurs at the acoustic impedance of the polystyrene substrate, which can be interpreted as an absence in the reflected signal as the acoustic impedance of the polystyrene substrate is equal to the acoustic impedance of the sample.

The results of the AIIM experiment and the fluorescence images of the three representative MCF-7 cells are illustrated in Figure 4. Whether the AIIM can be used to detect the presence of the nucleus could be related to the distance between the surface of the nucleus and the polystyrene substrate. In this case, there will be two consecutive acoustic impedance mismatches. The reflected signal caused by the mismatch between the cytoplasm and nucleus will interfere with the reflected signal caused by the mismatch between the polystyrene substrate and cytoplasm. This depends on the distance between the nucleus and the polystyrene substrate (Fig. 7b). The acoustic impedance mismatch detected between the cytoplasm and nucleus indicates the potential of the nucleus to be a scattering source in quantitative ultrasound analysis (QUS). Others have suggested the nucleus as the major scattering source in tissues with high cellular content (Czarnota et al. 1999; Kolios et al. 2003; Taggart et al. 2007). The average size ratio of the cytoplasm to the nucleus suggests that the highest acoustic impedance mismatch occurs between the medium and the cytoplasm.

Similar changes in acoustic impedance versus nucleus depth were observed for MCF-10 A cells. This supports the hypothesis that the nucleus is a potential scattering source within the cell. Using the AIIM to image more cells at different frequencies can potentially determine whether this interpretation of the data is correct, as the conditions for interference that create the variations seen in Figure 7b depend not only on the distance between the nucleus and the polystyrene substrate, but also on the wavelength of the ultrasound.

From the confocal images, the average distances of the nucleus to the polystyrene substrate in MCF-7 and MCF-10 A were 0.60 $\pm$ 1.40 and 0.35 $\pm$ 0.51 μm,

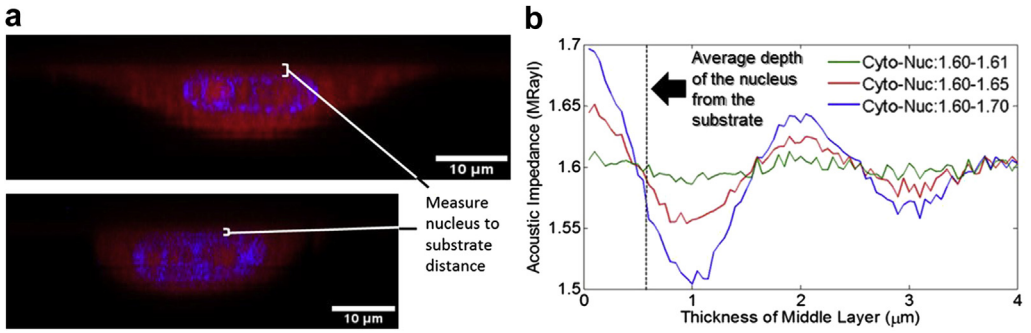

Fig. 7. (a) Cross-sectional image of two fixed MCF-7 cells imaged using confocal microscopy. The distances from the top of the cytoplasm (*red*, stained with CellTracker Orange) to the top of the nucleus (*blue*, stained with Hoechst) are 1 and 0.66 μm for the first and second cells, respectively. The average depth was measured to be 0.60 $\pm$ 1.40 μm. (b) Simulation of the measured acoustic impedance versus thickness of the middle layer. *Green, red and blue lines* are results of simulations 1, 2 and 3 from Table 1 ($\lambda = 4$ μm). The *dashed line* represents the average distance between the nucleus and the polystyrene substrate measured in the confocal microscopy experiments.

respectively (Fig. 7a). These results indicate the variation in the location of the nucleus with respect to the polystyrene substrate. COMSOL simulations correlate these changes to the measured acoustic impedance values using the AIIM (Fig. 7b). This can be connected back to Figures 4 and 5 to explain why acoustic impedance images were able to detect the presence of the nucleus in some images, as either an increase or a decrease in the acoustic impedance, and failed to detect the nucleus in other images. Future experiments will take the confocal measurements and the AIIM measurements on the same cells, so that the acoustic impedance variations can be correlated directly to the distance of the nucleus from the substrate.

Using the AIIM, we were able to measure the average acoustic impedance of normal and cancerous breast cells. The accuracy of the AIIM was verified by measuring the acoustic impedance of water with 0.33% error compared with the literature (Temkin 1981). The average acoustic impedance of single live cancer cells was calculated to be 1.612 ± 0.008 MRayl, which is higher than 1.56 ± 0.01 MRayl for MCF-7, previously obtained using time-resolved acoustic microscopy (Oelze and Mamou 2013; Strohm et al. 2010). The reason for the discrepancy may be that we were able to account for the acoustic impedance of the surrounding medium using the AIIM, which was not done in previous work. In the study by Strohm et al. (2010), the surrounding medium was assumed to have properties similar to those of water. The acoustic impedance value of cancer cells (HeLa) was measured to be 1.687 MRayl (Weiss et al. 2007), which is higher than the measured value for MCF-7 from this study. Others reported measured acoustic impedance values of normal cells of 1.53–1.94 and 1.785 MRayl using evaluation of $V(z)$ values and analysis of the generated voltage-versus-frequency curves, respectively (Kundu et al. 1991, 2000).

The main advantage of the AIIM over previous methods is its ability to measure the acoustic impedance maps of cells after accounting for the angle between the transducer and the cell surface (Fig. 1b). A high-resolution acoustic impedance map of a HeLa cell was acquired by Weiss et al. (2007). The cell was set on top of the substrate, which creates an angle between the cell surface and the transducer. Hildebrand and Rugar (1984) and Briggs et al. (1993) used a setup similar to that of Weiss et al. (2007) to measure a line profile acoustic impedance value of a single fibroblast. The angle of the transducer to the surface of the cell was not accounted for. In contrast, the AIIM does account for the angle, which in principle should lead to more accurate acoustic impedance measurements. This will provide a better interpretation of the QUS parameters (*e.g.*, effective scattering size and acoustic concentration), as the BSC is directly related to acoustic impedance values. The drawback of AIIM over time-resolved acoustic microscopy is the lower-contrast images. The ultrasound pulse has to pass through the polystyrene substrate first before it interferes with the cell. This reduces the amplitude of the detected signal and, therefore, reduces the contrast of the images.

Multiple observations have been noted using a multiple comparison test. First, a comparison of MCF-7 and MCF-10 A cells revealed that the average acoustic impedance value of MCF-10 A cells was significantly higher than that of MCF-7 cells. Knowledge that the acoustic impedance value of normal breast cells is higher than that of cancerous cells can be used in QUS to better assess the images, as mechanical properties are one of the inputs in QUS calculations. Second, comparison of the results for 3- and 7-μm erosion disks revealed a significant increase in the acoustic impedance value for the 7-μm erosion disk of single cells. This measured increase was less prominent for clustered cells. The increase is due mainly to the effect of the point spread function of the transducer. When the transducer is located above the boundary between the cell and the substrate, the resultant acoustic impedance values will be averaged. Because the background had a lower acoustic impedance value than the sample, the acoustic impedance values at the boundaries should be lower than the acoustic impedance of the sample. This was done to illustrate the importance of the size of the erosion disk (larger than the focal spot size) to more accurate measurement of acoustic impedance values of cells. Third, an increase, but not significant, in the average acoustic impedance of clustered versus single live cells was observed, as illustrated in Figure 6. One explanation is that clustered cells support more cell-to-cell interactions (*e.g.*, gap junctions), which allows various molecules and ions to pass between cells (Simek et al. 2009). The molecules and ions act as a signal for gene and protein expression which can lead to changes in cell physiology. In addition, the cells may potentially be overlapping, so the effect of the transducer point spread function is not as pronounced in the case of clustered cells. Finally, there is a decrease in the average acoustic impedance of fixed versus live cells, as illustrated in Figure 6. The purpose of measuring the acoustic impedance of fixed cells is to detect the effect of formalin on cell mechanical properties. Because in the future this method may be used on fixed clinical samples, it is important to note the effect of formalin fixation. Previous experiments report changes in density and speed of sound of fixed cells (Baldwin et al. 2005; Brayman and Miller 1993; Bryan et al. 2010).

To better understand the mechanical properties of cells using acoustic microscopy, several new analyses can be performed in the future. First, the AIIM could be used on the same cell using two different ultrasound pulse

wavelengths. Different pulse wavelengths will interfere in different ways, and the results can be used to acquire information about the depth of the nucleus. Second, higher-frequency transducers can be used to obtain higher-resolution acoustic impedance maps. Higher-resolution maps will make it possible to detect finer fluctuations in the acoustic impedance maps of cells.

CONCLUSIONS

Acoustic impedance images of normal (MCF-10 A) and cancerous (MCF-7) breast cells were obtained using the AIIM. With this technique, it was possible to differentiate between MCF-7 and MCF-10 A cells by comparing their average acoustic impedance values. The AIIM images were also linked to fluorescence and confocal images with stained nuclei and cytoplasm, which indicated that the depth of the nucleus has an impact on acoustic impedance images. In addition, the average acoustic impedance can be used to detect changes in the cell.

Acknowledgments—Funding for this work was provided by the Natural Sciences and Engineering Research Council of Canada (Discovery Grant 216986-2012) and a Terry Fox Foundation Program Project Grant entitled "Ultrasound and MRI for cancer therapy". Funding to purchase the equipment was provided by the Canada Foundation for Innovation, the Ontario Ministry of Research and Innovation, and Ryerson University.

REFERENCES

Ashkin A, Dziedzic JM. Optical trapping and manipulation of viruses and bacteria. Science 1987;235:1517–1520.

Baldwin SL, Yang M, Marutyan KR, Wallace KD, Holland MR, Miller JG. Measurements of the anisotropy of ultrasonic velocity in freshly excised and formalin-fixed myocardial tissue. J Acoust Soc Am 2005;118:505.

Bao G, Suresh S. Cell and molecular mechanics of biological materials. Nat Mater 2003;2:715–725.

Brayman AA, Miller MW. Cell density dependence of the ultrasonic degassing of fixed erythrocyte suspensions. Ultrasound Med Biol 1993;19:243–252.

Briggs GAD, Wang J, Gundle R. Quantitative acoustic microscopy of individual living human cells. J Microsc 1993;172:3–12.

Bryan AK, Goranov A, Amon A, Manalis SR, Kirschner MW. Measurement of mass, density, and volume during the cell cycle of yeast. Proc Natl Acad Sci U S A 2010;107:999–1004.

Carkaci S, Santiago L, Adrada BE, Whitman GJ. Screening for breast cancer with sonography. Semin Roentgenol 2011;46:285–291.

Chapman D. Mechanics and thermodynamics of biomembranes. FEBS Lett 1982;142:179–180.

Chesnick IE, Mason JT, O'Leary TJ, Fowler CB. Elevated pressure improves the rate of formalin penetration while preserving tissue morphology. J Cancer 2010;1:178–183.

Cobbold RSC. Foundations of biomedical ultrasound. New York: Oxford University Press; 2007.

Czarnota GJ, Kolios MC, Abraham J, Portnoy M, Ottensmeyer FP, Hunt JW, Sherar MD. Ultrasound imaging of apoptosis: High-resolution non-invasive monitoring of programmed cell death *in vitro, in situ* and *in vivo*. Br J Cancer 1999;81:520–527.

Falou O, Rui M, El Kaffas A, Kumaradas JC, Kolios MC. The measurement of ultrasound scattering from individual micron-sized objects and its application in single cell scattering. J Acoust Soc Am 2010;128:894–902.

Faran J. Sound scattering by solid cylinders and spheres. J Acoust Soc Am 1951;23:405.

Foster FS, Pavlin CJ, Harasiewicz KA, Christopher DA, Turnbull DH. Advances in ultrasound biomicroscopy. Ultrasound Med Biol 2000;26:1–27.

Fuchs E, Weber K. Intermediate filaments: Structure, dynamics, function and disease. Annu Rev Biochem 1994;63:345–382.

Gillespie JW, Strausberg RL, Epstein JI, Hamilton SR, Gannot G, Baibakova GV, Calvert VS, Flaig MJ, Chuaqui RF, Herring JC, Pfeifer J, Best CJM, Petricoin EF, Linehan WM, Duray PH, Bova GS, Emmert-Buck MR, Bichsel VE, Cole KA, Greenhut SF, Hewitt SM, Ahram M, Gathright YB, Merino MJ. Evaluation of non-formalin tissue fixation for molecular profiling studies. Am J Pathol 2002;160:449–457.

Hildebrand JA, Rugar D. Measurement of cellular elastic properties by acoustic microscopy. J Microsc 1984;134(Pt 3):245–260.

Hozumi N, Hozumi N, Nakano A, Nakano A, Terauchi S, Nagao M, Yoshida S, Kobayashi K, Yamamoto S, Saijo Y. 9D-1 precise calibration for biological acoustic impedance microscope. IEEE Ultrason Symp 2007;801–804.

Hozumi N, Kimura A, Terauchi S, Nagao M, Yoshida S, Kobayashi K, Saijo Y. Acoustic impedance micro-imaging for biological tissue using a focused acoustic pulse with a frequency range up to 100 MHz. Proc IEEE Ultrason Symp 2005;1:170–173.

Hruska DP, Sanchez J, Oelze ML. Improved diagnostics through quantitative ultrasound imaging. New York: IEEE; 2009. p. 1956–1959.

Ingber DE. Mechanical signaling and the cellular response to extracellular matrix in angiogenesis and cardiovascular physiology. Circ Res 2002;91:877–887.

Insana MF, Wood JG, Hall TJ. Identifying acoustic scattering sources in normal renal parenchyma *in vivo* by varying arterial and ureteral pressures. Ultrasound Med Biol 1992;18:587.

Kemmerer J, Ghoshal G, Oelze M. Quantitative ultrasound assessment of HIFU induced lesions in rodent live. Proc IEEE Ultrason Symp 2010;1396–1469.

Kolios M. Biomedical ultrasound imaging from 1 to 1000 MHz. Can Acoust 2009;37:35–43.

Kolios MC, Czarnota GJ, Lee M, Hunt JW, Sherar MD. Ultrasonic spectral parameter characterization of apoptosis. Ultrasound Med Biol 2002;28:589–597.

Kolios MC, Taggart L, Baddour R, Foster F, Hunt J, Czarnota G, Sherar M. An investigation of backscatter power spectra from cells, cell pellets and microspheres. Proc IEEE Ultrason Symp 2003;1:752–757.

Kundu T, Bereiter-Hahn J, Hillmann K. Measuring elastic properties of cells by evaluation of scanning acoustic microscopy *V(Z)* values using simplex algorithm. Biophys J 1991;59:1194–1207.

Kundu T, Bereiter-Hahn J, Karl I. Cell property determination from the acoustic microscope generated voltage versus frequency curves. Biophys J 2000;78:2270–2279.

Lizzi FL, Greenebaum M, Feleppa EJ, Elbaum E, Coleman DJ. Theoretical framework for spectrum analysis in ultrasonic tissue characterization. J Acoust Soc Am 1983;73:1366.

Lizzi FL, Ostromogilsky M, Feleppa EJ, Rorke MC, Yaremko MM. Relationship of ultrasonic spectral parameters to features of tissue microstructure. IEEE Trans Ultrason Ferroelectr Freq Control 1987;34:319–329.

Maev RG. Acoustic microscopy: Fundamentals and applications. Weinheim: Wiley-VCH; 2008.

Mamou J, Feleppa EJ, Coron A, Oelze ML, Saegusa-Beecroft E, Hata M, Lee P, Machi J, Yanagihara E, Laugier P. Three-dimensional high-frequency backscatter and envelope quantification of cancerous human lymph nodes. Ultrasound Med Biol 2011;37:345–357.

Mamou J, Oelze ML, O'Brien J, William D, Zachary JF. Extended three-dimensional impedance map methods for identifying ultrasonic scattering sites. J Acoust Soc Am 2008;123:1195–1208.

Mamou J, Oelze ML, O'Brien J, William D, Zachary JF. Identifying ultrasonic scattering sites from three-dimensional impedance maps. J Acoust Soc Am 2005;117:413.

Mathis G, (ed). Chest sonography. 3rd ed. New York: Springer; 2011.

Mayer WG. Energy partition of ultrasonic waves at flat boundaries. Ultrasonics 1965;3:62–68.

Oelze ML, Mamou J. Quantitative ultrasound in soft tissues. Dordrecht: Springer; 2013.
Oelze ML, O'Brien J, William D, Blue JP, Zachary JF. Differentiation and characterization of rat mammary fibroadenomas and 4T1 mouse carcinomas using quantitative ultrasound imaging. New York: IEEE; 2004. p. 764–771.
Oelze ML, Zachary JF. Examination of cancer in mouse models using high-frequency quantitative ultrasound. Ultrasound Med Biol 2006;32:1639–1648.
Puig-De-Morales M, Grabulosa M, Alcaraz J, Mullol J, Maksym GN, Fredberg JJ, Navajas D. Measurement of cell microrheology by magnetic twisting cytometry with frequency domain demodulation. J Appl Physiol 2001;91:1152–1159.
Radmacher M, Fritz M, Hansma PK. Imaging soft samples with the atomic force microscope: Gelatin in water and propanol. Biophys J 1995;69:264–270.
Simek J, Churko J, Shao Q, Laird DW. Cx43 has distinct mobility within plasma-membrane domains, indicative of progressive formation of gap-junction plaques. J Cell Sci 2009;122:554–562.
Strohm E, Czarnota GJ, Kolios MC. Quantitative measurements of apoptotic cell properties using acoustic microscopy. IEEE Trans Ultrason Ferroelectr Freq Control 2010;57:2293–2304.
Suresh S, Spatz J, Mills JP, Micoulet A, Dao M, Lim CT, Beil M, Seufferlein T. Connections between single-cell biomechanics and human disease states: Gastrointestinal cancer and malaria. Acta Biomater 2005;1:15–30.
Taggart LR, Baddour RE, Giles A, Czarnota GJ, Kolios MC. ultrasonic characterization of whole cells and isolated nuclei. Ultrasound Med Biol 2007;33:389–401.
Temkin S. Elements of acoustics. New York: Wiley; 1981.
Tohno E, Ueno E, Watanabe H. Ultrasound screening of breast cancer. Breast Cancer 2009;16:18–22.
Usami S, Chen HH, Zhao Y, Chien S, Skalak R. Design and construction of a linear shear stress flow chamber. Ann Biomed Eng 1993;21:77–83.
Wang JH, Goldschmidt-Clermont P, Yin FC. Contractility affects stress fiber remodeling and reorientation of endothelial cells subjected to cyclic mechanical stretching. Ann Biomed Eng 2000;28:1165–1171.
Wear KA. Ultrasonic characterization of the heart (myocardium). ProQuest, UMI Dissertations. Stanford University, California, United States, 1987.
Weiss EC, Anastasiadis P, Pilarczyk G, Lemor RM, Zinin PV. Mechanical properties of single cells by high-frequency time-resolved acoustic microscopy. IEEE Trans Ultrason Ferroelectr Freq Control 2007;54:2257–2271.
Zhao X, Akhtar R, Nijenhuis N, Wilkinson SJ, Murphy L, Ballestrem C, Sherratt MJ, Watson REB, Derby B. Multi-layer phase analysis: Quantifying the elastic properties of soft tissues and live cells with ultra-high-frequency scanning acoustic microscopy. IEEE Trans Ultrason Ferroelectr Freq Control 2012;59:610–620.

APPENDIX

The parameters in eqn (5) (T_{c-PE}, R_{PE-s}, R_{PE-r}, T_{PE-c}) to account for the shear wave created in the polystyrene substrate and the transducer directivity can be calculated using the following equations (Mayer 1965):

$$T_{c-PE} = \frac{2\sqrt{BC_1}}{1+C_1(1-2A)}$$

$$A = \sin(\theta_{PE_t})\sin(2\theta_{PE_t})\left[\cos(\theta_{PE_t}) - \left(\frac{c_{PE_t}}{c_{PE_l}}\right)\cos(\theta_{PE_l})\right]$$

$$B = (\cos(2\theta_{PE_t}))^2, C_1 = \frac{Z_{PE_l}\cos(\theta_a)}{Z_c\cos(\theta_{PE_l})}$$

$$R_{PE-s} = \frac{E-F-C_s}{E+F+C_s}, R_{PE-r} = \frac{E-F-C_r}{E+F+C_r}$$

$$C_s = \frac{Z_s\cos(\theta_{PE_l})}{Z_{PE_l}\cos(\theta_s)}, C_r = \frac{Z_r\cos(\theta_{PE_l})}{Z_{PE_l}\cos(\theta_r)}$$

$$E = (\cos(2\theta_{PE_t}))^2, F = \left(\frac{c_{PE_t}}{c_{PE_l}}\right)^2 \sin(2\theta_{PE_l})\sin(2\theta_{PE_t})$$

$$T_{PE-c} = \frac{\sqrt{4EC_2}}{E+F+C_2}$$

$$C_2 = \frac{Z_c\cos(\theta_{PE_l})}{Z_{o_l}\cos(\theta_a)}$$

The subscripts t and l represent the transverse and longitudinal waves, and the subscripts PE, c, r and s represent the polystyrene substrate, coupling fluid, reference and sample. The angles are calculated from the aperture angle (θ_a) using Snell's law:

$$\theta_{PE_l} = \arcsin\left(\frac{c_{PE_l}}{c_c}\sin(\theta_a)\right), \theta_{PE_t} = \arcsin\left(\frac{c_{PE_t}}{c_{PE_l}}\sin(\theta_{PE_l})\right)$$

$$\theta_s = \arcsin\left(\frac{c_s}{c_{PE_l}}\sin(\theta_{PE_l})\right), \theta_r = \arcsin\left(\frac{c_r}{c_{PE_l}}\sin(\theta_{PE_l})\right)$$